Supplementary Information (SI) for Environmental Science: Nano.

Supporting Information

Cobalt doping of FeS_2 simultaneously promotes radical and nonradical pathways of O_2 activation by creating dual active sites

Fangru He [a], Meimei Shen [a], Zongsheng Liang [a], Jingxiang Low [b], Tong Zhang *[a], Wei Chen *[a], Chuanjia Jiang *[a]

[a] *Ministry of Education Key Laboratory of Pollution Processes and Environmental Criteria, Tianjin Key Laboratory of Environmental Remediation and Pollution Control, College of Environmental Science and Engineering, Nankai University, Tianjin 300350, China*

[b] *School of Physical Science and Technology, Tiangong University, Tianjin, 300387, China*

* Corresponding authors:

E-mail: zhangtong@nankai.edu.cn (T. Zhang); chenwei@nankai.edu.cn (W. Chen); jiangcj@nankai.edu.cn (C. Jiang)

Number of pages: 39

Number of figures: 18

Number of tables: 11

Text S1 Chemical and regents

Ferrous sulfate heptahydrate ($FeSO_4·7H_2O$, 99.99%), cobaltous sulfate heptahydrate ($CoSO_4·7H_2O$, 99.99%), urea (99.5%), *N,N*-dimethylformamide (99.5%), ethylene glycol (99.0%), ethanol (99.8%), trichloroethylene (TCE, 99.5%), 2,4,6-trichlorophenol (2,4,6-TCP, 99.5%), ciprofloxacin (CIP, 99.5%), sulfamethoxazole (SMX, 99.5%), tert-butanol (TBA, 99.8%), furfural (FFA, 99.8%), methanol (MeOH, 99.8%), *p*-benzoquinone (*p*-BQ, 99.5%), L-histidine (L-his, 99.5%), potassium thiocyanate (KSCN, 99.5%), benzoic acid (BA, 99.5%), *p*-hydroxybenzoic acid (*p*-HBA, 99.5%), methyl phenyl sulfoxide (PMSO, 98%), methyl phenyl sulfone ($PMSO_2$, 99%), *5-tert*-butoxycarbonyl-5-methyl-1-pyrroline *N*-oxide (BMPO, 99 %), and 2,2,6,6-tetra methyl-1-piperidinyloxy (TEMP, 98%) were acquired from Aladdin Corporation (Shanghai, China). Sublimed sulfur (S, > 99.99%) was purchased from Alfa Aesar Corporation (Shanghai, China). Humic acid (HA) was purchased from Sigma-Aldrich (Shanghai, China). Deionized water (18 MΩ cm at 25 °C) from a Millipore water purification system was used throughout the experiments. All chemicals and reagents were used without further purification.

Text S2 Preparation of materials

Synthesis of FeS_2. FeS_2 was successfully synthesized via a solvothermal method.[1] 2 mmol of $FeSO_4·7H_2O$ and 10 mmol of urea were initially dissolved in a mixed solvent comprising 30 mL of *N,N*-dimethylformamide and 40 mL of ethylene glycol. Subsequently, 25 mmol of sublimed sulfur was added to the solution. After stirring for 1 h, the suspension was transferred to a 100-mL Teflon-lined stainless-steel autoclave, which was then tightly sealed and maintained at 180 °C for 12 h. The resulting product was centrifuged and thoroughly washed with deionized water and absolute ethanol. The black solid was then dried for 12 h in a freezer drier.

Synthesis of Co-doped FeS_2. Co-doped FeS_2 was synthesized using the above procedure except that a specified amount of $CoSO_4\cdot 7H_2O$ was added (with the amount of $FeSO_4\cdot 7H_2O$ decreased correspondingly). The molar ratio of $FeSO_4\cdot 7H_2O$ and $CoSO_4\cdot 7H_2O$ was set to 0.98:0.02, 0.95:0.05, and 0.90:0.10, and the corresponding samples were labeled as $Co_{0.02}$-FeS_2, $Co_{0.05}$-FeS_2, and $Co_{0.10}$-FeS_2, respectively.

Text S3 Material characterization

X-ray diffraction (XRD, Ultima IV, Rigaku, Japan) was used to verify the crystal structure of FeS_2 and Co-doped FeS_2 materials. Raman spectroscopy measurement was conducted on a RM2000 microscope system (Renishaw, England) using an excitation wavelength of 532 nm. Electron paramagnetic resonance (E580-10/12, Beuker, Germany) spectroscopy was used to detect the defect sites. X-ray photoelectron spectroscopy (XPS, ESCALAB 250Xi, Thermo Scientific, U.S.A) was used to analyze the chemical state of surface elements. Elemental content was determined by inductively coupled plasma-optical emission spectroscopy (ICP-OES, OPTIMA 8300, Perkin-Elmer, U.S.A). Morphology of the materials was characterized by a field-emission scanning electron microscopy (SEM, JSM-2100F, JEOL, Japan) and a field-emission transmission electron microscopy (TEM, JEOL JEM-2800, Japan). The energy-dispersive X-ray spectroscopy (EDS) elemental mapping was also obtained on the JEOL JEM-2800 instrument. The Brunauer−Emmett−Teller specific surface area of the materials was measured by nitrogen adsorption–desorption on a Micromeritics ASAP 2460 system (Micromeritics, Norcross, U.S.A.).

Text S4 Pollutant degradation experiments

Degradation experiments of pollutants (2,4,6-TCP, TCE, CIP, and SMX) were conducted in 20-mL serum bottles in the dark, with a shaking rate of 180 rpm at a constant temperature of 25

°C. In a typical degradation experiment, 10 mg of a material was added to the bottle, followed by the addition of 10 mL of the pollutant solution to initiate the reaction. The pH of the pollutant solution was adjusted to 7 (or 3 and 9) using 1 M NaOH and 1 M H_2SO_4 prior to the experiment. The bottle was then sealed with an aluminum cap containing a PTFE silicone septum. For TCE analysis, three parallel samples were sacrificed to analyze the residual TCE concentration at designated time intervals. For analysis of 2,4,6-TCP, CIP, and SMX, 0.5 mL of suspension was withdrawn and then mixed with 1 mL of methanol. The mixture was filtered through a 0.22-μm nylon filter membrane for further analysis. Using the above procedures, the performances of the materials for degrading 2,4,6-TCP and TCE were also evaluated under a nitrogen (N_2) atmosphere, in simulated groundwater, and in the presence of HA. For the quenching experiments, 0.1 mL of quenchers (e.g., TBA, L-his, and KSCN) were added to the system, and its effect on the total volume was negligible. In the cyclic experiments, the materials were separated by high-speed centrifugation (10000 rpm), and the supernatant was carefully discarded. Fresh pollutant solutions (2,4,6-TCP and TCE) were then added to initiate the experiments.

A subset of experiments were performed in simulated groundwater (pH = 7.2, ionic strength = 3.78 mmol/L), which was prepared following a previously reported method.[2] In brief, 60 mg of $MgSO_4 \cdot 7H_2O$, 20 mg of KNO_3, 36 mg of $NaHCO_3$, 36 mg of $CaCl_2$, 35 mg of $Ca(NO_3)_2$, and 25 mg of $CaSO_4 \cdot 2H_2O$ were dissolved in 1 L of deoxygenated deionized water.

Text S5 ROS quantification methods

The •OH radical was quantified using BA as the probe. The accumulative concentration of •OH ($[\bullet OH]_{acc}$) was estimated according to the yield of *p*-HBA ($[\bullet OH]_{acc} \approx 5.87 \times [p\text{-HBA}]$).[3] The steady-state concentration of $^1O_2$ ($[^1O_2]_{ss}$) was measured using FFA as the probe.[4] Since

FFA also has a higher reactivity with •OH, MeOH was added to exclude the interference of •OH ($k_{\mathrm{MeOH,\bullet OH}} = 9.7 \times 10^8$ $M^{-1}s^{-1}$; $k_{\mathrm{MeOH,O2\bullet-}} < 0.01$ $M^{-1}s^{-1}$; $k_{\mathrm{MeOH,1O2}} = 3.89 \times 10^3$ $M^{-1}s^{-1}$).[5,6] Subsequently, the steady-state concentration of $^1O_2$ was calculated from the degradation kinetics of FFA, as shown in eq 1, 2. The production of Fe(IV) was evaluated by analyzing the conversion efficiency of PMSO to $PMSO_2$.[7,8]

$$\frac{d[FFA]}{dt} =- k_{FFA,1O2} \times [FFA][^1O_2]_{ss}$$

(1)

$$\frac{ln\frac{[FFA]}{[FFA]_0}}{t} =- k_{FFA,1O2} \times [^1O_2]_{ss}$$

(2)

where $[FFA]_0$ represents the initial concentration of the FFA at time $t = 0$. [FFA] represents the concentration of the FFA at a specific time t. $k_{\mathrm{FFA,1O2}}$ equals to 3.8×10^8 $M^{-1}s^{-1}$ [4].

Text S6 Procedures for TCE analysis

The concentration of TCE in headspace was obtained using a gas chromatograph (GC, Shimadzu 2014, Japan) equipped with a flame ionization detector (FID, Shimadzu 2014, Japan). The chromatographic column used was HP-PLOT/Q (30 m × 0.32 mm × 20 μm). The temperature of the headspace sampler's constant temperature furnace was set at 85 °C, which was held constant for 20 min, and the transmission line temperature was 105 °C. The injector temperature for the GC-FID was 150 °C, and the detector temperature was 220 °C. The column flow rate was 1 mL min^{-1}, with a split ratio of 10:1. The temperature program for the chromatographic column was set at 50 °C for 2 min, then an increase at a rate of 10 °C min^{-1} to 220 °C and held for 6 min.

Text S7 Theoretical calculations

The projected augmented wave (PAW) potentials were applied to describe the ionic cores and take valence electrons into account using a plane wave basis set with a kinetic energy cutoff of 450 eV. Partial occupancies of the Kohn–Sham orbitals were allowed using the Gaussian smearing method and a width of 0.05 eV. The electronic energy was considered self-consistent when the energy change was smaller than 10^{-5} eV. A geometry optimization was considered convergent when the force change was smaller than 0.05 eV/Å. In our structure, the U correction was used for Fe (4.65 eV) atoms. Grimme's DFT-D3 methodology was used to describe the dispersion interactions. The vacuum spacing perpendicular to the plane of the structure was 20 Å. The Brillouin zone integral utilized the surfaces structures of 3 × 3 × 1 monkhorst pack K-point sampling. The (200) crystal plane was selected as the model surface, because XRD results indicated that the (200) crystal plane was the predominant exposed facet for both FeS_2 and the Co-FeS_2 materials (Table S11).

The adsorption energy (E_{ads}) was obtained using eq 3:

$$E_{\mathrm{ads}} = E_{\mathrm{ad/sub}} - E_{\mathrm{ad}} - E_{\mathrm{sub}} \tag{3}$$

where $E_{\mathrm{ad/sub}}$ is the total energy of the optimized adsorbate/substrate system, E_{ad} is the substrate's energy, and E_{sub} is the energy of the free adsorbate molecules.

The Gibbs free energy (ΔG) was calculated using eq 4:

$$\Delta G = \Delta E + \Delta E_{\mathrm{ZPE}} - T\Delta S \tag{4}$$

where ΔE, ΔE_{ZPE}, and $T\Delta S$ are the total energy, zero-point energy difference, and entropic contributions, respectively.

The differential charge density was obtained using eq 5:

$$\Delta\rho = \rho_{\mathrm{O2+materials}} - (\rho_{\mathrm{materials}} + \rho_{\mathrm{O2}}) \tag{5}$$

where $\rho_{\mathrm{O2+materials}}$ represents the charge density of the adsorbed system, $\rho_{\mathrm{materials}}$ represents the charge density of FeS_2 or Co-doped FeS_2, and ρ_{O2} represents the charge density of a single O_2 molecule.

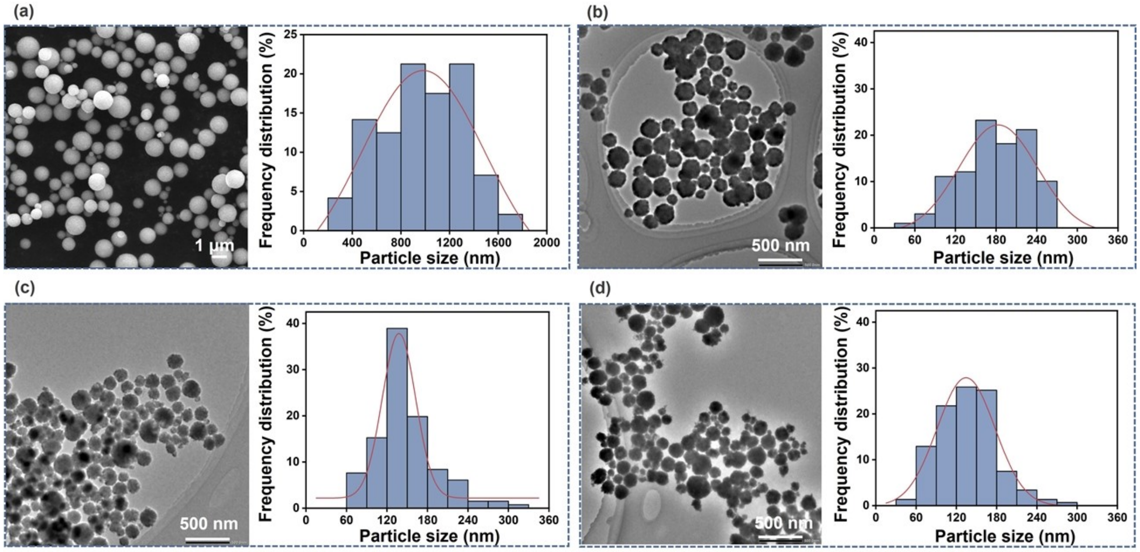

Figure S1. SEM/TEM images and particle size distribution patterns of (a) FeS_2, (b) $Co_{0.02}$-FeS_2, (c) $Co_{0.05}$-FeS_2, and (d) $Co_{0.10}$-FeS_2.

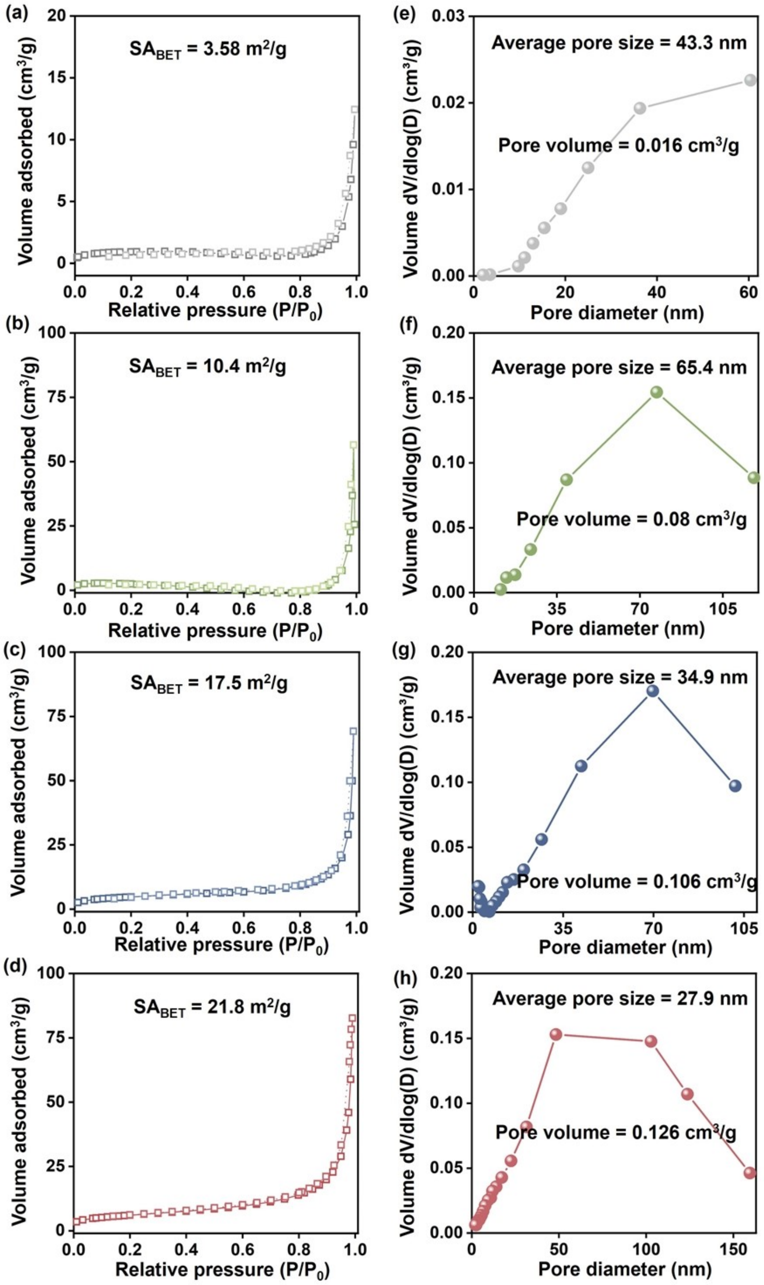

Figure S2. N_2 adsorption and desorption isotherms of (a) FeS_2, (b) $Co_{0.02}$-FeS_2, (c) $Co_{0.05}$-FeS_2, and (d) $Co_{0.10}$-FeS_2. Pore size distribution patterns of (e) FeS_2, (f) $Co_{0.02}$-FeS_2, (g) $Co_{0.05}$-FeS_2, and (h) $Co_{0.10}$-FeS_2.

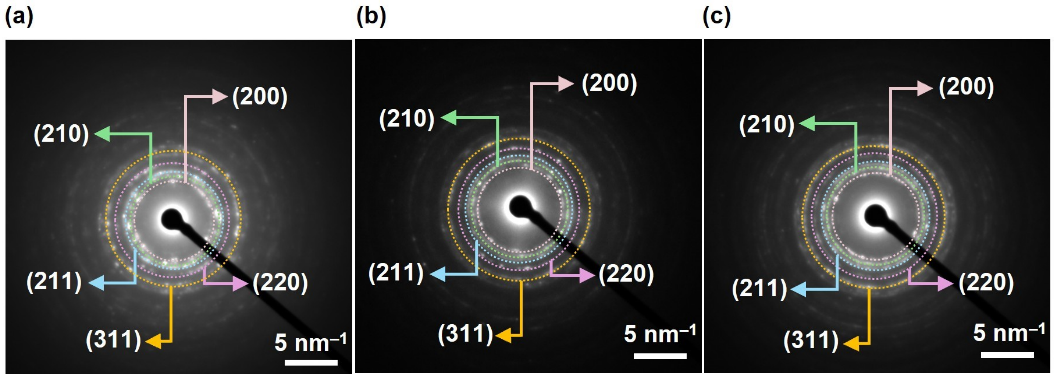

Figure S3. Selected area electron diffraction patterns of (a) $Co_{0.02}$-FeS_2, (b) $Co_{0.05}$-FeS_2, and (c) $Co_{0.10}$-FeS_2.

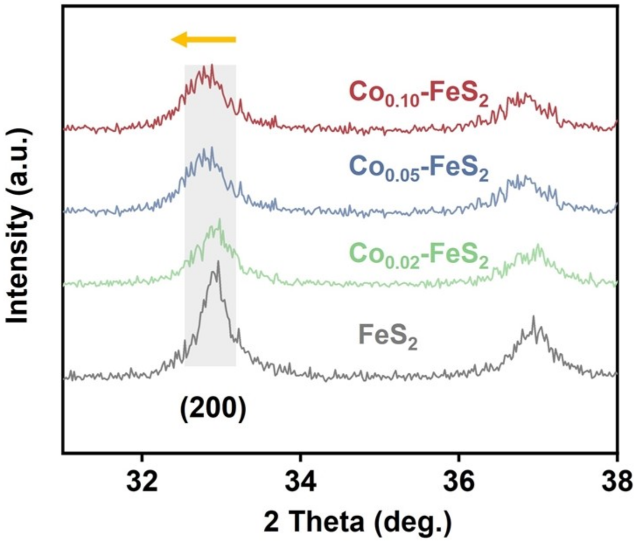

Figure S4. XRD patterns of different materials at low diffraction angles of 31° to 38°.

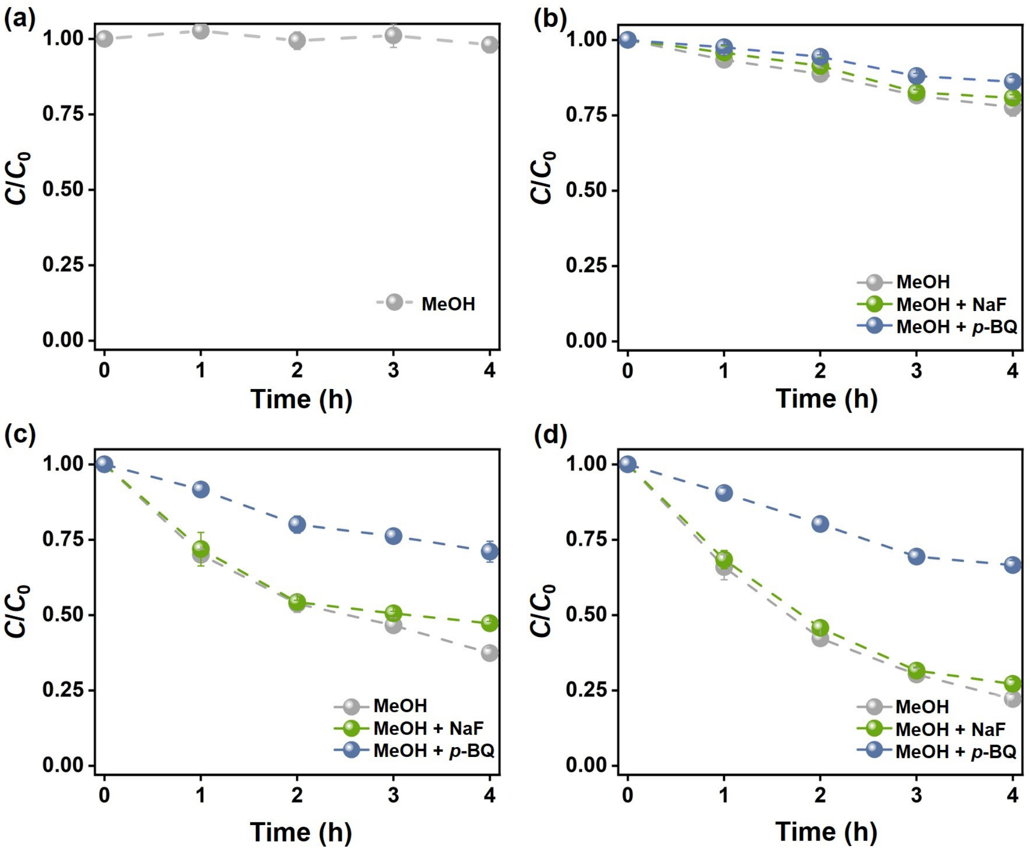

Figure S5. The degradation curves of FFA in the (a) FeS_2, (b) $Co_{0.02}$-FeS_2, (c) $Co_{0.05}$-FeS_2, and (d) $Co_{0.10}$-FeS_2 systems with the different scavengers. [Materials] = 1 g/L, [FFA] = 50 μmol/L, [MeOH] = 2 mM, [*p*-BQ] = 2 mM, [NaF] = 2 mM, initial pH = 7.

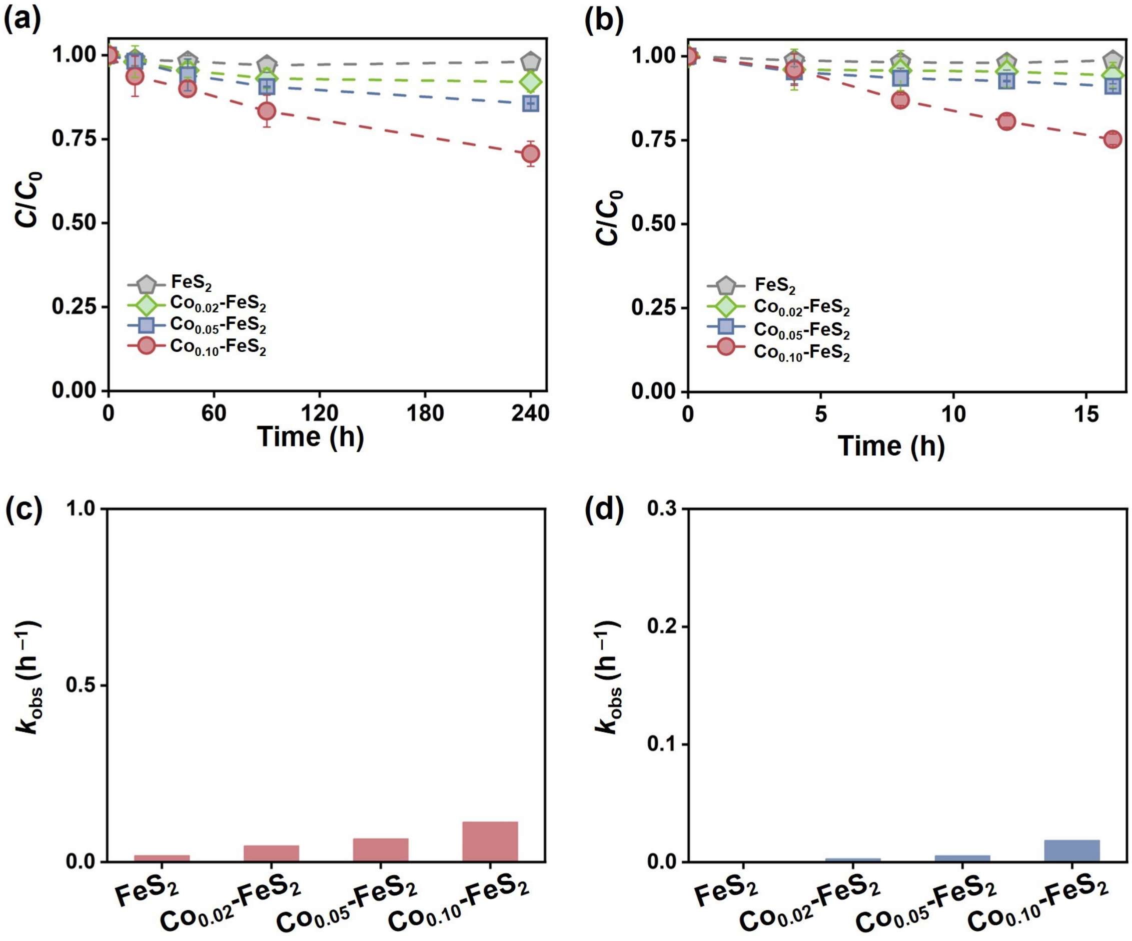

Figure S6. The degradation curves of (a) 2,4,6-TCP and (b) TCE by the materials in DI water under N_2 atmosphere. Conditions: [Materials] = 1 g/L, [2,4,6-TCP] = 4 mg/L, [TCE] = 1 mg/L, initial pH = 7. The apparent rate constants (k_{obs}) for degradation of (c) 2,4,6-TCP and (d) TCE by the materials.

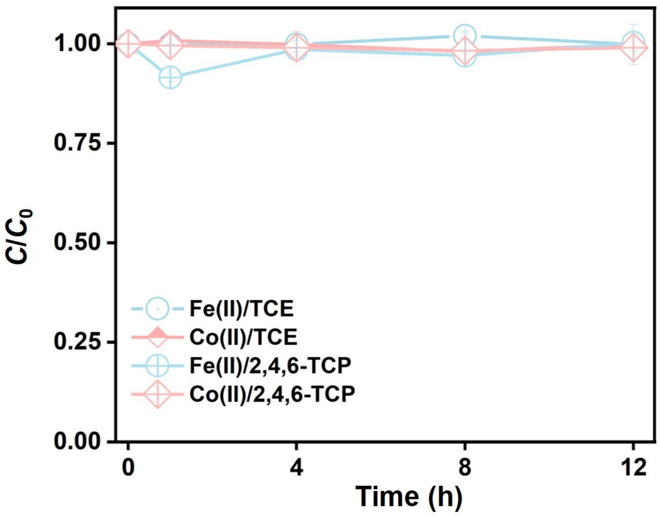

Figure S7. The degradation curves of TCE and 2,4,6-TCP in the Co^{2+}/Fe^{2+}-mediated O_2 activation. [Co^{2+}] = 5 mg/L, [Fe^{2+}] = 50 mg/L, [TCE] = 1 mg/L, [2,4,6-TCP] = 4 mg/L, initial pH = 3. The concentration of Co^{2+} and Fe^{2+} was chosen based on the total leached ion concentrations measured after 16 h of reaction in $Co_{0.10}$-FeS_2 system under aerobic conditions. The concentration of total dissolved Co ions detected in the solution is 3.6 mg/L, while the concentration of total dissolved Fe ions is 38.9 mg/L.

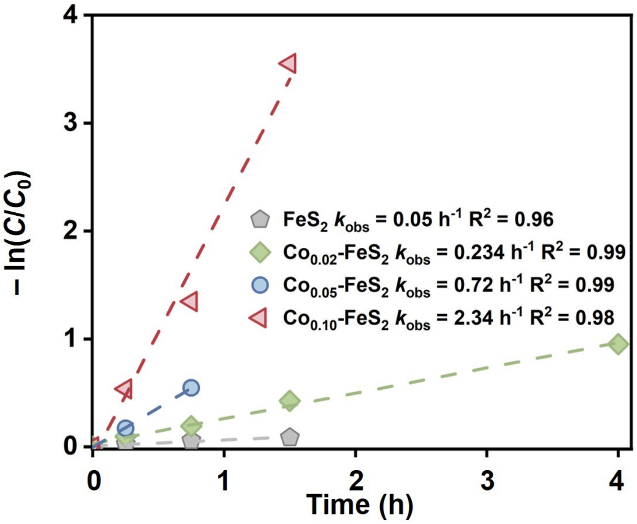

Figure S8. The fitted pseudo-first-order kinetics of 2,4,6-TCP degradation by the materials in DI water. Conditions: [Materials] = 1 g/L, [2,4,6-TCP] = 4 mg/L, initial pH = 7.

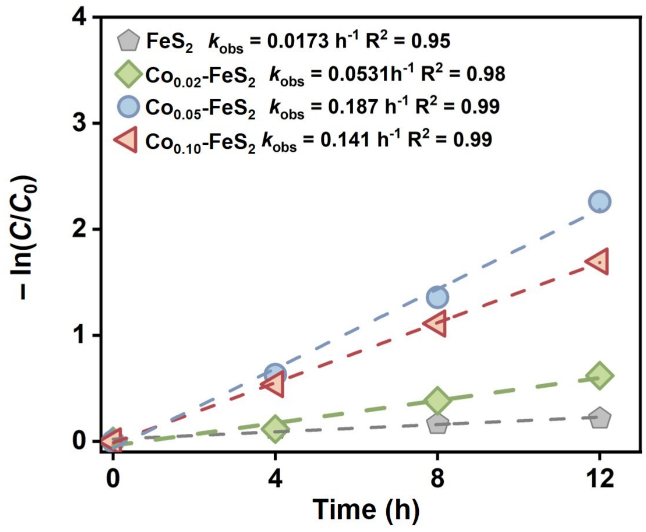

Figure S9. The fitted pseudo-first-order kinetics of TCE degradation by the materials in DI water. Conditions: [Materials] = 1 g/L, [TCE] = 1 mg/L, initial pH = 7.

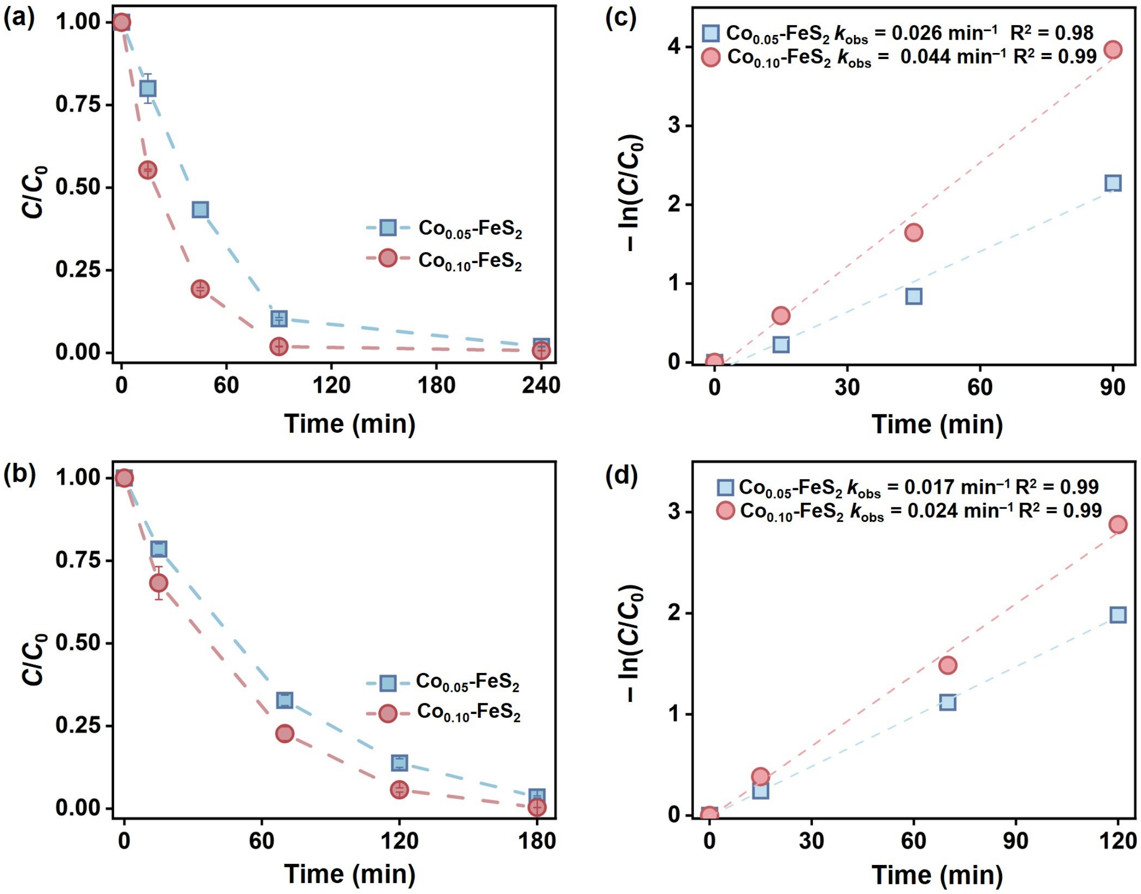

Figure S10. The degradation curves of (a) CIP and (b) SMX. The fitted pseudo-first-order kinetics of (c) CIP and (d) SMX degradation. Conditions: [Materials] = 1 g/L, [CIP] = [SMX] = 4 mg/L, initial pH = 7.

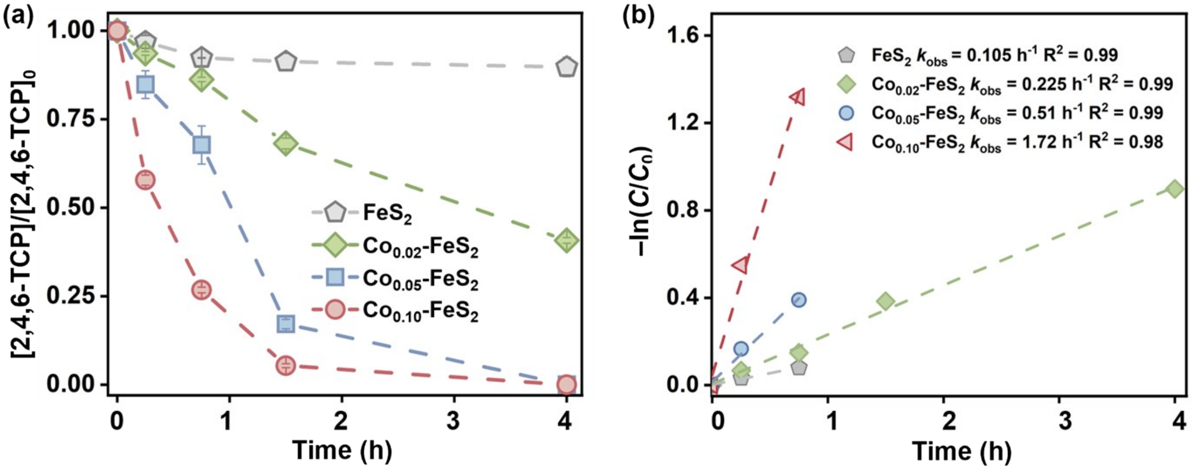

Figure S11. (a) The degradation curves and (b) the fitted pseudo-first-order kinetics of 2,4,6-TCP degradation by the materials in simulated groundwater. Conditions: [Materials] = 1 g/L, [2,4,6-TCP] = 4 mg/L, initial pH = 7.2.

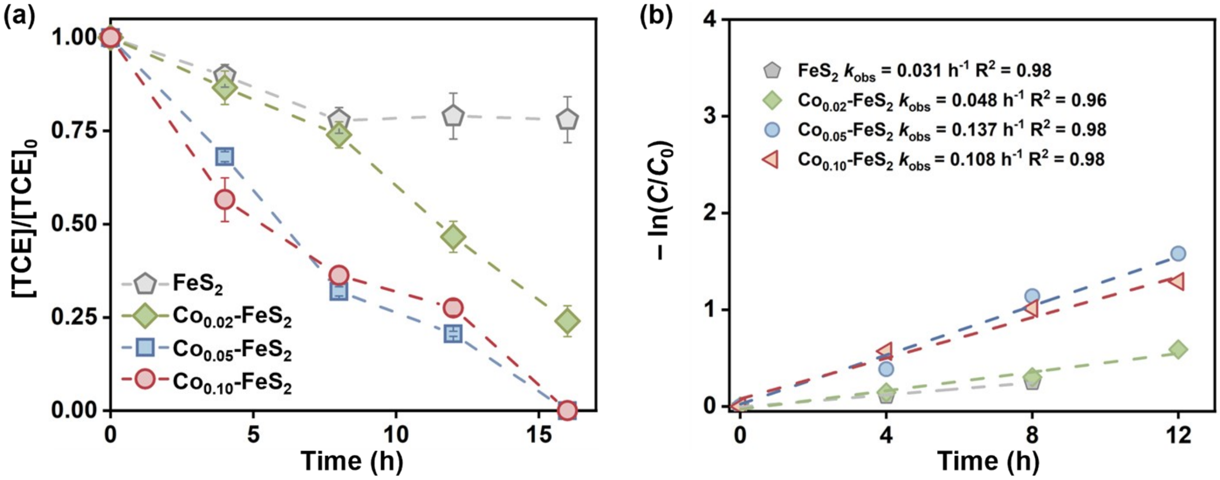

Figure S12. (a) The degradation curves and (b) the fitted pseudo-first-order kinetics of TCE degradation by the materials in simulated groundwater. Conditions: [Materials] = 1 g/L, [TCE] = 1 mg/L, initial pH = 7.2.

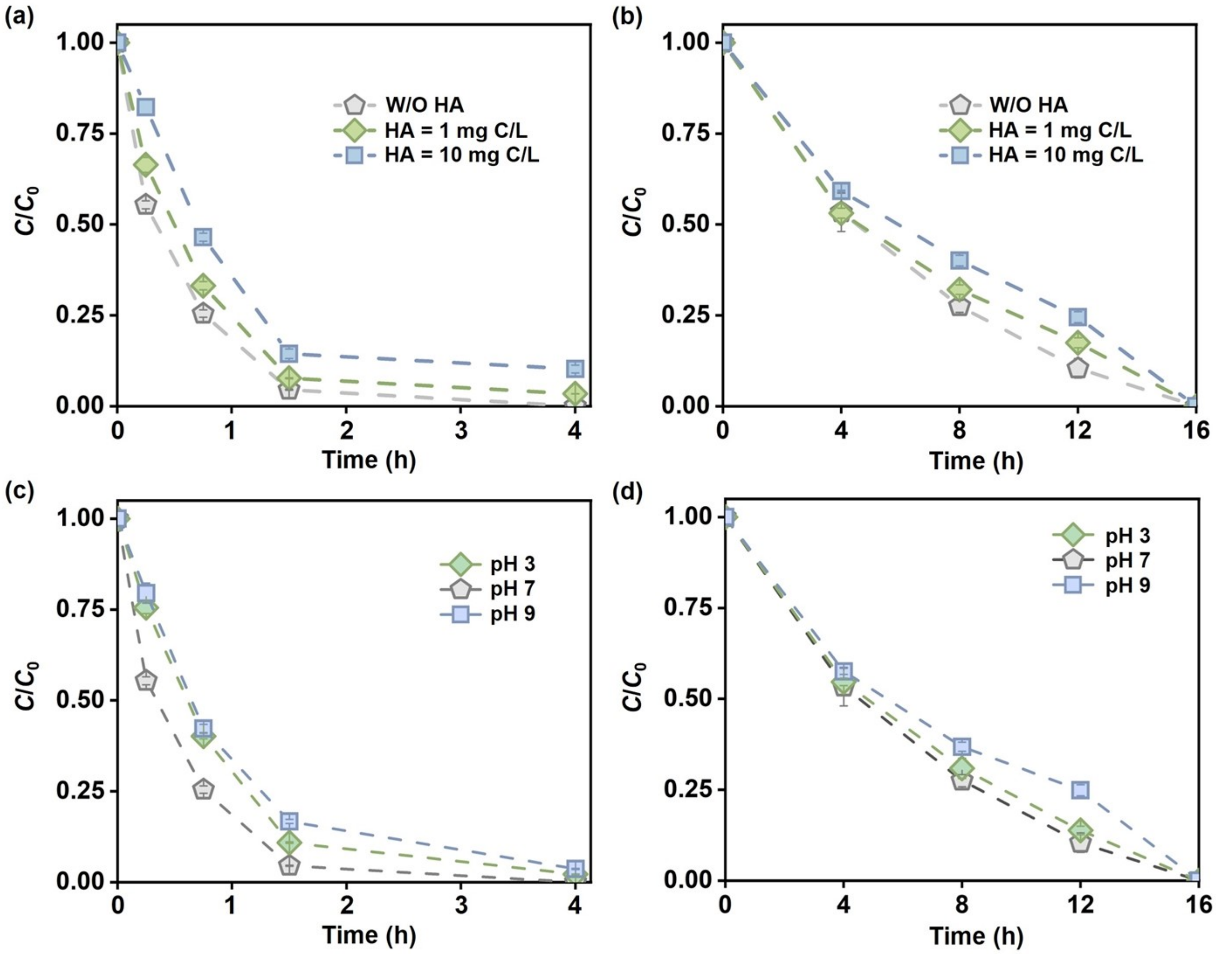

Figure S13. Degradation curves of (a) 2,4,6-TCP and (b) TCE in the presence or absence of HA. Degradation curves of (c) 2,4,6-TCP and (d) TCE under different pH conditions. Conditions: [Materials] = 1 g/L, [2,4,6-TCP] = 4 mg/L, [TCE] = 1 mg/L.

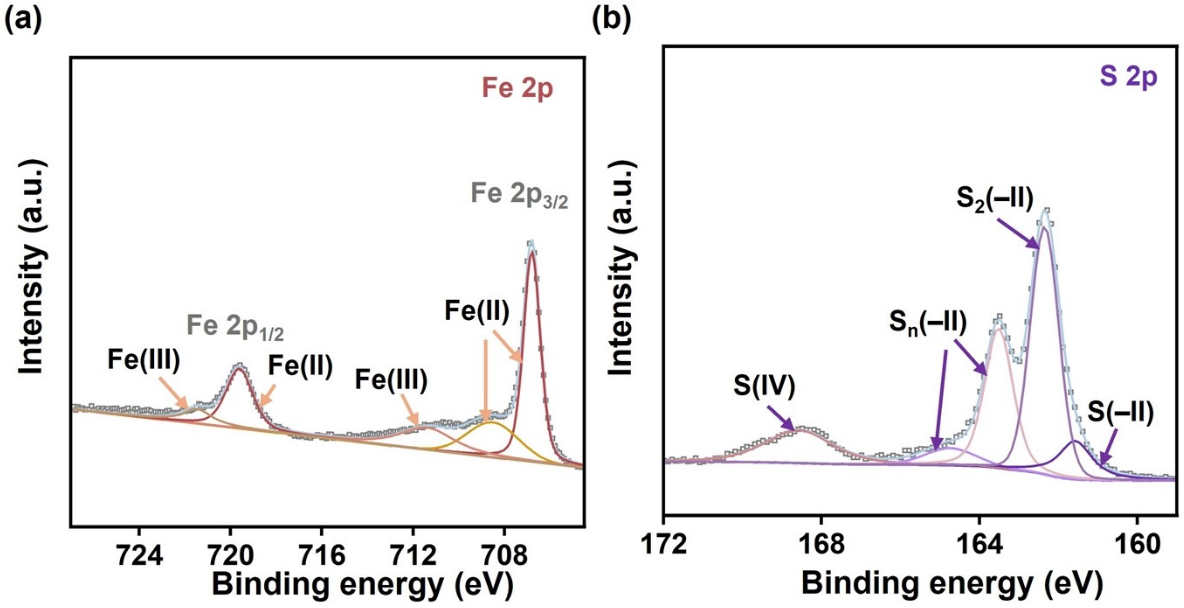

Figure S14. XPS spectra of (a) Fe 2p and (b) S 2p of FeS_2. The component peaks at 707 and 709 eV correspond to the Fe $2p_{3/2}$ orbital of Fe(II), while the peak at 720 eV corresponds to the Fe $2p_{1/2}$ orbital of Fe(II). The component peaks at approximately 711 and 721 eV are attributed to the $2p_{3/2}$ and Fe $2p_{1/2}$ orbitals of Fe(III).[9] The component peaks at approximately 161, 162, 163, 165, and 169 eV are assigned S(–II), S_2(–II), S_n(–II), S_n(–II), and S(IV), respectively.[10]

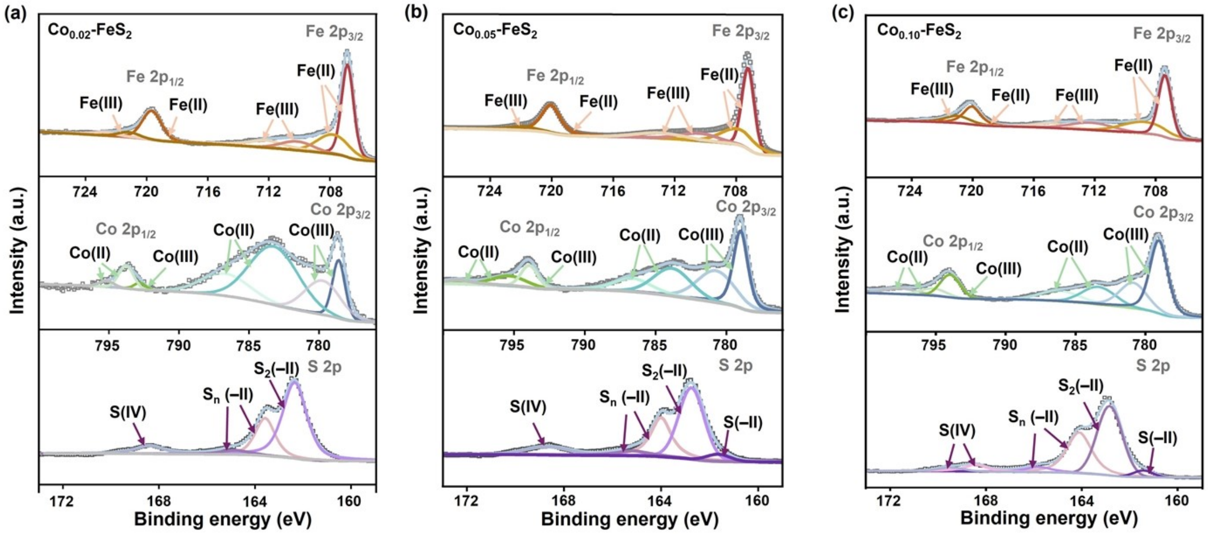

Figure S15. XPS spectra of Fe 2p, Co 2p, and S 2p of (a) $Co_{0.02}$-FeS_2, (b) $Co_{0.05}$-FeS_2, and (c) $Co_{0.10}$-FeS_2. The component peaks at 707 and 708 eV correspond to the Fe $2p_{3/2}$ orbital of Fe(II), while the peak at 720 eV corresponds to the Fe $2p_{1/2}$ orbital of Fe(II). The component peaks at 710 and 712 eV correspond to the Fe $2p_{3/2}$ orbital of Fe(III), while the peak at 721 eV corresponds to the Fe $2p_{1/2}$ orbital of Fe(III).[9] The component peaks at approximately 161, 163, 164, 165, 168, and 169 eV are assigned S(–II), S_2(–II), S_n(–II), S_n(–II), S(IV), and S(IV), respectively.[10] The component peaks at 779 eV and 780 eV correspond to the Co $2p_{3/2}$ orbital of Co(III), while the peak at 793 eV correspond to the Co $2p_{1/2}$ orbital of Co(III). The component peaks at 783 eV and 787 eV correspond to the Co $2p_{3/2}$ orbital of Co(II), while the peak at 794 eV and 796 correspond to the Co $2p_{1/2}$ orbital of Co(II).[11]

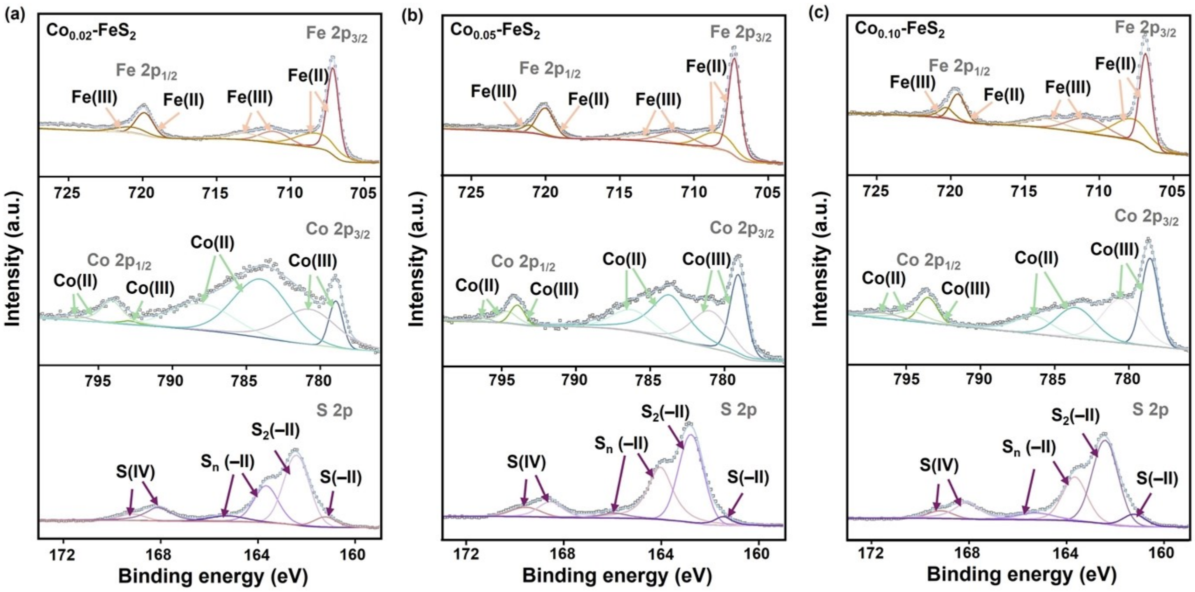

Figure S16. XPS spectra of Fe 2p, Co 2p, and S 2p of (a) $Co_{0.02}$-FeS_2, (b) $Co_{0.05}$-FeS_2, and (c) $Co_{0.10}$-FeS_2 after 16-h reaction. The component peaks at 707 and 708 eV correspond to the Fe $2p_{3/2}$ orbital of Fe(II), while the peak at 720 eV corresponds to the Fe $2p_{1/2}$ orbital of Fe(II). The component peaks at 710 and 712 eV correspond to the Fe $2p_{3/2}$ orbital of Fe(III), while the peak at 721 eV corresponds to the Fe $2p_{1/2}$ orbital of Fe(III).[9] The component peaks at approximately 161, 163, 164, 165, 168, and 169 eV are assigned S(–II), S_2(–II), S_n(–II), S_n(–II), S(IV), and S(IV), respectively.[10] The component peaks at 779 eV and 780 eV correspond to the Co $2p_{3/2}$ orbital of Co(III), while the peak at 793 eV correspond to the Co $2p_{1/2}$ orbital of Co(III). The component peaks at 783 eV and 787 eV correspond to the Co $2p_{3/2}$ orbital of Co(II), while the peak at 794 eV and 796 correspond to the Co $2p_{1/2}$ orbital of Co(II).[11]

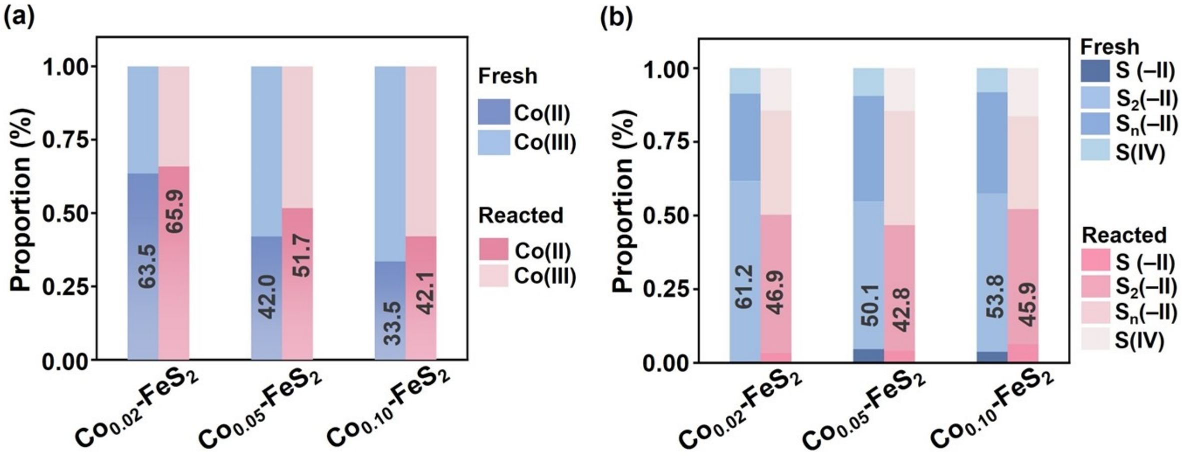

Figure S17. The proportion of (a) Co species and (b) S species on the surface of the materials before and after 16-h reaction.

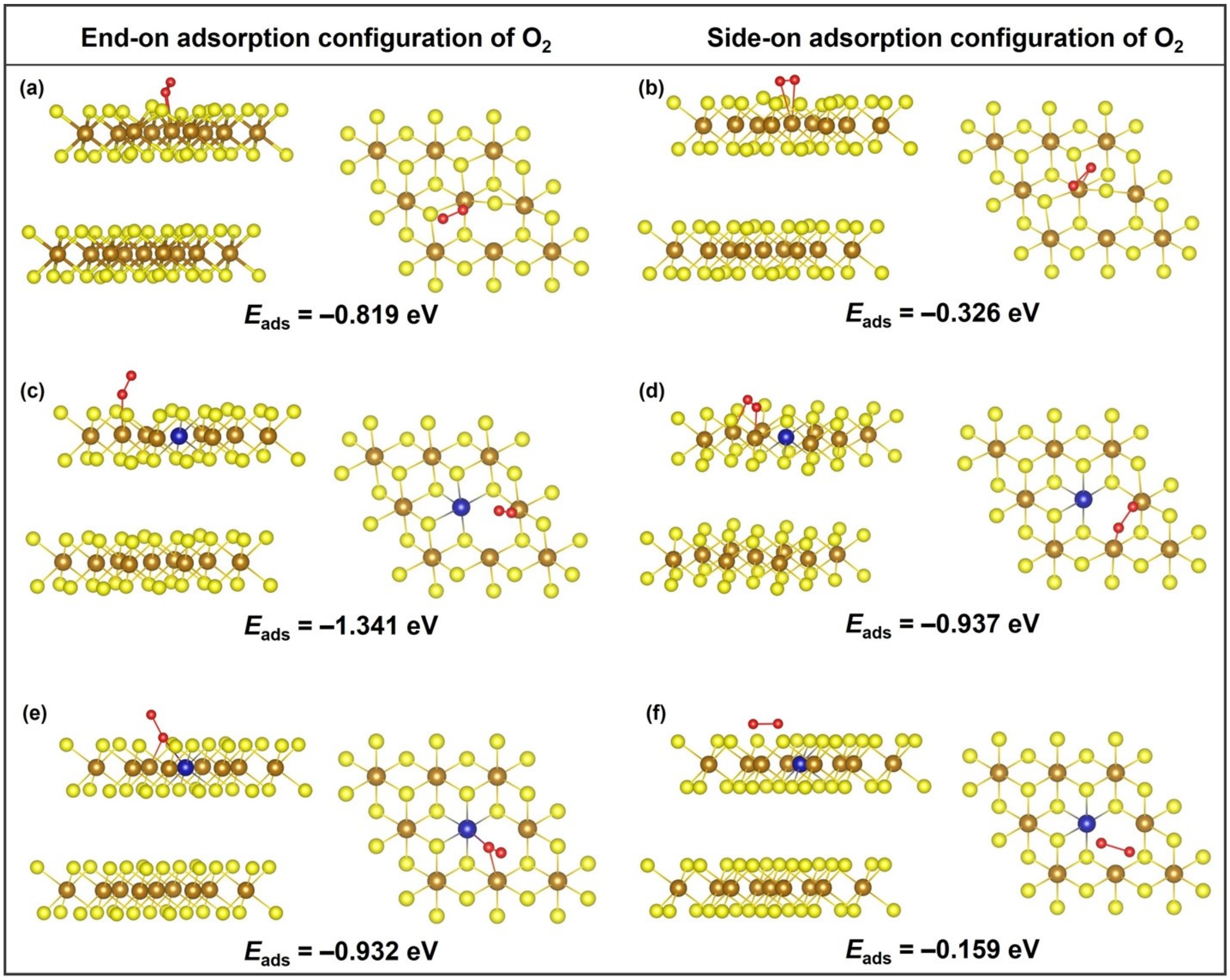

Figure S18. O_2 adsorption energy in (a, c, e) end-on or (b, d, f) side-on adsorption configuration at different sites: (a, b) Fe site in FeS_2, (c, d) Fe site in Co-doped FeS_2, and (e, f) SV site in Co-doped FeS_2.

Table S1. The high-performance liquid chromatography analysis parameters.

Substrates	Flow rate (mL/min)	λ (nm)	Mobile phase composition	Ref.
2,4,6-TCP	1	280	MeOH:H_2O = 85:15	[12]
CIP	1	276	MeOH:H_2O = 85:15	[13]
SMX	1	270	MeOH:0.1% acetic acid = 60:40	[14]
p-HBA	1	255	acetonitrile:0.1% trifluoroacetic acid = 65:35	[15]
FFA	1	219	MeOH:H_2O = 20:80	[16]
PMSO	1	235	MeOH:0.1% trifluoroacetic acid = 50:50	[14]
$PMSO_2$	1	215	MeOH:0.1% trifluoroacetic acid = 50:50	[14]

Table S2. The Co/Fe ratio of the Co-FeS_2 materials.

Materials	Co/Fe ratio (theoretical)	Co/Fe ratio (obtained from ICP-OES)	Co/Fe ratio (obtained from EDS)
$Co_{0.02}$-FeS_2	1:49	1:57.5	1:57
$Co_{0.05}$-FeS_2	1:19	1:20.4	1:19
$Co_{0.10}$-FeS_2	1:9	1:9.5	1:10

Table S3. The d spacing of different materials.

Facet	$Co_{0.02}$-FeS_2 (nm)	$Co_{0.05}$-FeS_2 (nm)	$Co_{0.10}$-FeS_2 (nm)	Pyrite PDF #97-000-0316 (nm)
(111)	-	0.290	0.311	0.313
(200)	0.278	0.278	0.280	0.271
(210)	0.252	0.249	0.247	0.243
(211)	0.223	0.225	0.226	0.222
(220)	0.194	0.200	0.196	0.192
(311)	0.167	0.166	-	0.164

Notes: Date obtained from selected area electron diffraction patterns (Fig. S3).

Table S4. Summary of rate constants of organic pollutant degradation by Fe-based materials-mediated O_2 activation.

Pollutants	Material	Dose (g/L)	Pollutants	Conditions	k_{obs} (h^{-1})	Ref.
Phenols	FeS	1	Phenol	Initial pH = 7.0, $[\text{Phenol}]_0$ = 53.1 μM	0.21	[3]
	Pyrite	0.5	phenol	Initial pH = 7.0, $[\text{Phenol}]_0$ = 1 μM	0.08	[17]
	Pyrite	0.5	BPA	Initial pH = 7.0, $[\text{BPA}]_0$ = 1 μM	0.14	[17]
	FeS/OA	0.5	BPA	Initial pH = 7.0, $[\text{BPA}]_0$ = 44 μM	0.69	[18]
	FeS/GA	0.5	BPA	Initial pH = 7.0, $[\text{BPA}]_0$ = 44 μM	0.17	[18]
	FeS/TA	0.5	BPA	Initial pH = 7.0, $[\text{BPA}]_0$ = 44 μM	0.10	[18]
	FeS/AA	0.5	BPA	Initial pH = 7.0, $[\text{BPA}]_0$ = 44 μM	0.07	[18]
	$Fe@Fe_2O_3$	11.2	4-CP	Initial pH = 6.0, $[\text{4-CP}]_0$ = 1.1 mM	0.22	[19]
	$Co\text{-}FeS_2$	1	2,4,6-TCP	Initial pH = 7.0, $[\text{2,4,6-TCP}]_0$ = 4 mg/L	2.3	This study
Chlorinated hydrocarbons	Pyrite	20 m^2/L	TCE	Initial pH = 6.0, $[\text{TCE}]_0$ = 0.62 mM	0.013	[20]
	FeS	1	TCE	Initial pH = 7.0, $[\text{TCE}]_0$ = 5 mg/L	0.12	[3]
	$Co\text{-}FeS_2$	1	TCE	Initial pH = 7.0, $[\text{TCE}]_0$ = 1 mg/L	0.19	This study
Antibiotics	SV-pyrite	1	SMX	Initial pH = 8.5, $[\text{SMX}]_0$ = 1 mg/L	0.17	[21]
	$Co\text{-}Fe_3S_4$	0.5	SMX	Initial pH = 5.0, $[\text{SMX}]_0$ = 10 mg/L	0.0019	[22]
	Pyrite	0.5	CBZ	Initial pH = 7.0, $[\text{CBZ}]_0$ = 1 μM	0.10	[17]
	S-FeS	0.1	CIP	Initial pH = 9.0, $[\text{CIP}]_0$ = 1 mg/L	0.78	[23]
	$Co\text{-}FeS_2$	1	SMX	Initial pH = 7.0, $[\text{SMX}]_0$ = 4 mg/L	1.4	This study
	$Co\text{-}FeS_2$	1	CIP	Initial pH = 7.0, $[\text{CIP}]_0$ = 4 mg/L	2.6	This study

Notes: k_{obs}: the degradation rate constant of pollutants. BPA: bisphenol A. 4-CP: 4-chlorophenol. TCE: trichloroethylene. SMX: sulfamethoxazole. CIP: ciprofloxacin. CBZ: carbamazepine. OA: oxalic acid. GA: galic acid. TA: tartaric acid. AA: ascorbic acid.

Table S5. XPS fitting parameters of Fe 2p of fresh materials.

Sample	Orbitals	Bind energy (eV)	FWHM (eV)	Area (CPS eV^{-1})	Assignment	Atomic (%)
FeS_2	Fe $2p_{3/2}$	706.8	0.88	38546	Fe(II)	77.8
	Fe $2p_{3/2}$	708.5	2.6	16690		
	Fe $2p_{1/2}$	719.6	1.4	18065		
	Fe $2p_{3/2}$	711.0	2.1	14906	Fe(III)	7.3
	Fe $2p_{1/2}$	721.4	1.5	5994		
$Co_{0.02}$-FeS_2	Fe $2p_{3/2}$	706.8	0.93	94193	Fe(II)	75.9
	Fe $2p_{3/2}$	707.8	2.4	46800		
	Fe $2p_{1/2}$	719.6	1.5	46719		
	Fe $2p_{3/2}$	710.1	2.5	21896	Fe(III)	24.1
	Fe $2p_{3/2}$	712.2	2.8	29819		
	Fe $2p_{1/2}$	721.2	1.6	7990		
$Co_{0.05}$-FeS_2	Fe $2p_{3/2}$	707.2	0.94	76904	Fe(II)	77.2
	Fe $2p_{3/2}$	707.8	2.6	40110		
	Fe $2p_{1/2}$	720.0	1.4	49078		
	Fe $2p_{3/2}$	710.4	2.9	20157	Fe(III)	22.8
	Fe $2p_{3/2}$	712.9	3.6	17710		
	Fe $2p_{1/2}$	721.8	2.1	11085		
$Co_{0.10}$-FeS_2	Fe $2p_{3/2}$	707.4	1.0	77659	Fe(II)	70.0
	Fe $2p_{3/2}$	708.7	3.4	45793		
	Fe $2p_{1/2}$	720.0	1.3	34914		
	Fe $2p_{3/2}$	712.0	3.3	28110	Fe(III)	30.0
	Fe $2p_{3/2}$	714.8	2.4	19694		
	Fe $2p_{1/2}$	721.0	2.0	20365		

Notes: FWHM, full width at half maximum; CPS, counts per second.

Table S6. XPS fitting parameters of Fe 2p of materials after the reaction.

Sample	Orbitals	Bind energy (eV)	FWHM (eV)	Area (CPS eV^{-1})	Assignment	Atomic (%)
$Co_{0.02}$-FeS_2	Fe $2p_{3/2}$	707.1	0.93	65184	Fe(II)	74.0
	Fe $2p_{3/2}$	708.1	3.2	33561		
	Fe $2p_{1/2}$	719.8	1.3	22681		
	Fe $2p_{3/2}$	711.0	2.2	18429	Fe(III)	26.0
	Fe $2p_{3/2}$	712.9	2.7	13553		
	Fe $2p_{1/2}$	720.7	2.5	10624		
$Co_{0.05}$-FeS_2	Fe $2p_{3/2}$	707.2	0.95	72154	Fe(II)	72.8
	Fe $2p_{3/2}$	708.5	2.6	29362		
	Fe $2p_{1/2}$	720.0	1.3	25985		
	Fe $2p_{3/2}$	711.3	2.6	23775	Fe(III)	27.2
	Fe $2p_{3/2}$	713.5	2.9	14493		
	Fe $2p_{1/2}$	721.1	1.2	9325		
$Co_{0.10}$-FeS_2	Fe $2p_{3/2}$	706.8	0.95	40033	Fe(II)	66.4
	Fe $2p_{3/2}$	707.8	2.9	27051		
	Fe $2p_{1/2}$	719.5	1.2	13531		
	Fe $2p_{3/2}$	710.8	3.0	19677	Fe(III)	33.6
	Fe $2p_{3/2}$	713.5	3.0	14070		
	Fe $2p_{1/2}$	720.3	1.2	7100		

Table S7. XPS fitting parameters of Co 2p of fresh materials.

Sample	Orbitals	Bind energy (eV)	FWHM (eV)	Area (CPS eV^{-1})	Assignment	Atomic (%)
$Co_{0.02}$-FeS_2	Co $2p_{3/2}$	783.2	4.1	41222	Co(II)	63.5
	Co $2p_{3/2}$	786.7	4.0	15829		
	Co $2p_{1/2}$	793.7	1.2	4845		
	Co $2p_{1/2}$	795.2	1.2	1208		
	Co $2p_{3/2}$	778.6	3.0	17523	Co(III)	36.5
	Co $2p_{3/2}$	779.8	3.0	17528		
	Co $2p_{1/2}$	792.8	0.97	1251		
$Co_{0.05}$-FeS_2	Co $2p_{3/2}$	783.8	3.1	30543	Co(II)	42.0
	Co $2p_{3/2}$	786.6	3.1	17051		
	Co $2p_{1/2}$	795.3	2.9	10753		
	Co $2p_{1/2}$	798.9	2.4	4610		
	Co $2p_{3/2}$	779.0	1.2	38979	Co(III)	58.0
	Co $2p_{3/2}$	780.7	3.1	36768		
	Co $2p_{1/2}$	793.9	1.3	11015		
$Co_{0.10}$-FeS_2	Co $2p_{3/2}$	783.3	2.8	28948	Co(II)	33.5
	Co $2p_{3/2}$	786.1	3.3	21042		
	Co $2p_{1/2}$	795.2	2.2	9259		
	Co $2p_{1/2}$	797.5	2.9	9713		
	Co $2p_{3/2}$	779.0	1.4	74404	Co(III)	66.5
	Co $2p_{3/2}$	780.9	2.3	39460		
	Co $2p_{1/2}$	793.9	1.7	23262		

Table S8. XPS fitting parameters of Co 2p of materials after the reaction.

Sample	Orbitals	Bind energy (eV)	FWHM (eV)	Area (CPS eV^{-1})	Assignment	Atomic (%)
$Co_{0.02}$-FeS_2	Co $2p_{3/2}$	783.9	4.3	33049	Co(II)	65.9
	Co $2p_{3/2}$	787.9	5.0	16948		
	Co $2p_{1/2}$	793.9	1.8	7000		
	Co $2p_{1/2}$	796.5	2.0	1291		
	Co $2p_{3/2}$	778.9	1.1	6594	Co(III)	34.1
	Co $2p_{3/2}$	780.7	4.4	22674		
	Co $2p_{1/2}$	792.9	1.4	945		
$Co_{0.05}$-FeS_2	Co $2p_{3/2}$	783.6	3.0	31573	Co(II)	51.7
	Co $2p_{3/2}$	786.3	3.2	13862		
	Co $2p_{1/2}$	794.5	1.4	4582		
	Co $2p_{1/2}$	796.2	1.2	1069		
	Co $2p_{3/2}$	779.0	1.3	20772	Co(III)	48.3
	Co $2p_{3/2}$	780.9	3.0	22962		
	Co $2p_{1/2}$	793.9	1.1	3936		
$Co_{0.10}$-FeS_2	Co $2p_{3/2}$	783.5	3.0	22924	Co(II)	42.1
	Co $2p_{3/2}$	786.4	3.0	16120		
	Co $2p_{1/2}$	794.6	2.3	8105		
	Co $2p_{1/2}$	796.6	3.0	5220		
	Co $2p_{3/2}$	778.5	1.4	28448	Co(III)	57.9
	Co $2p_{3/2}$	780.5	3.0	34590		
	Co $2p_{1/2}$	793.5	1.5	9000		

Table S9. XPS fitting parameters of S 2p of fresh materials.

Sample	Bind energy (eV)	FWHM (eV)	Area (CPS eV^{-1})	Assignment	Atomic (%)
FeS_2	161.5	1.0	7296	S(–II)	10.3
	162.3	0.9	29897	S_2(–II)	42.3
	163.5 164.7	0.9 1.5	18642 3840	S_n(–II)	31.9
	168.5	2.0	10932	S(IV)	15.5
$Co_{0.02}$-FeS_2	161.4	0.5	864	S(–II)	0.4
	162.4	1.2	125074	S_2(–II)	61.2
	163.6 164.8	1.0 1.4	51111 9463	S_n(–II)	29.7
	168.4	1.4	17731	S(IV)	8.7
$Co_{0.05}$-FeS_2	161.6	1.2	9297	S(–II)	4.6
	162.7	1.2	100505	S_2(–II)	50.1
	164.0 165.1	1.0 1.6	59828 12323	S_n(–II)	35.9
	168.7	2.1	18982	S(IV)	9.4
$Co_{0.10}$-FeS_2	161.6	1.0	8011	S(–II)	3.7
	162.9	1.3	114983	S_2(–II)	53.8
	164.2 165.8	1.0 2.0	61286 12001	S_n(–II)	34.3
	168.4 169.4	1.2 1.2	10969 6463	S(IV)	8.2

Table S10. XPS fitting parameters of S of materials after the reaction.

Sample	Bind energy (eV)	FWHM (eV)	Area (CPS eV^{-1})	Assignment	Atomic (%)
$Co_{0.02}$-FeS_2	161.5	0.9	5243	S(–II)	3.3
	162.6	1.1	74421	S_2(–II)	46.9
	163.8	1.0	43742	S_n(–II)	35.4
	165	1.3	12281		
	168.4	1.2	9978	S(IV)	14.4
	169.2	1.6	12764		
$Co_{0.05}$-FeS_2	161.5	0.8	7127	S(–II)	4.0
	162.8	1.2	76140	S_2(–II)	42.8
	164.0	1.2	61641	S_n(–II)	38.7
	165.9	1.4	7347		
	168.5	1.2	15929	S(IV)	14.5
	169.6	1.5	9869		
$Co_{0.10}$-FeS_2	161.2	1.1	9013	S(–II)	6.3
	162.4	1.3	65853	S_2(–II)	45.9
	163.7	1.2	35999	S_n(–II)	31.5
	165.2	1.8	9186		
	168.1	1.3	17645	S(IV)	16.3
	169.1	1.2	5817		

Table S11. Facet proportions of different materials.

Facets	FeS_2	$Co_{0.02}$-FeS_2	$Co_{0.05}$-FeS_2	$Co_{0.10}$-FeS_2
(111)	15.1	11.8	11.6	12.6
(200)	23.6	20.9	22.0	19.3
(210)	18.3	18.1	19.5	19.8
(211)	13.9	14.8	16.0	12.3
(220)	16.8	20.1	15.2	19.8
(311)	12.3	14.3	15.7	16.2

Note: Date obtained from XRD results and the calculation method follows the approach described in the literature.[17]

References

1 K. Zhang, M. Park, L. Zhou, G.-H. Lee, J. Shin, Z. Hu, S.-L. Chou, J. Chen and Y.-M. Kang, *Angew. Chem. Int. Ed.*, 2016, **55**, 12822–12826.

2 I. Chowdhury, M. C. Duch, N. D. Mansukhani, M. C. Hersam and D. Bouchard, *Environ. Sci. Technol.*, 2013, **47**, 6288–6296.

3 D. Cheng, A. Neumann, S. Yuan, W. Liao and A. Qian, Oxidative Degradation of Organic Contaminants by FeS in the Presence of O_2, *Environ. Sci. Technol.*, 2020, **54**, 4091–4101.

4 Y. Lei, Y. Yu, X. Lei, X. Liang, S. Cheng, G. Ouyang and X. Yang, Assessing the Use of Probes and Quenchers for Understanding the Reactive Species in Advanced Oxidation Processes, *Environ. Sci. Technol.*, 2023, **57**, 5433–5444.

5 J. Liang, L. Fu, K. Gao and X. Duan, Accelerating radical generation from peroxymonosulfate by confined variable Co species toward ciprofloxacin mineralization: ROS quantification and mechanisms elucidation, *Appl. Catal. B*, 2022, **315**, 121542.

6 L. Gao, Y. Guo, J. Zhan, G. Yu and Y. Wang, Assessment of the validity of the quenching method for evaluating the role of reactive species in pollutant abatement during the persulfate-based process, *Water Res.*, 2022, **221**, 118730.

7 M. Li, H. Li, C. Ling, H. Shang, H. Wang, S. Zhao, C. Liang, C. Mao, F. Guo, B. Zhou, Z. Ai and L. Zhang, Highly selective synthesis of surface $Fe^{IV}=O$ with nanoscale zero-valent iron and chlorite for efficient oxygen transfer reactions, *P. Natl. Acad. Sci. U.S.A.*, 2023, **120**, e2304562120.

8 B. Yang, H. Liu and J. Zhang, High-valent metals in advanced oxidation processes: A critical review of their identification methods, formation mechanisms, and reactivity performance, *Chem. Eng. J.*, 2023, **460**, 141796.

9 Y. Liu, X. Sheng, Z. Zhou, P. Wang, Z. Lu, J. Dong, Y. Sun and S. Lyu, Efficient naphthalene degradation in FeS_2-activated nano calcium peroxide system: Performance and mechanisms, *J. Hazard. Mater.*, 2022, **432**, 128693.

10 J. Li, J. Lu, X. Lu, B. Tu, B. Ouyang, X. Han, and R Wang, Sulfur Transformation in Microbially Mediated Pyrite Oxidation by Acidithiobacillus ferrooxidans: Insights From X-ray Photoelectron Spectroscopy-Based Quantitative Depth Profiling, *Geomicrobiol. J.*, 2015, 1041182.

11 Y. Liu, C. Liu, X. Peng, Z. Liang, S. Hou, W. Chen and T. Zhang, Modulating d-orbital electronic configuration of magnetic iron sulfide nanocrystals for maximized treatment efficiency of chromium-contaminated water, *Water Res.*, 2025, **280**, 123477.

12 H. Li, S. Li, L. Jin, Z. Lu, M. Xiang, C. Wang, W. Wang, J. Zhang, C. Li and H. Xie, Activation of peroxymonosulfate by magnetic Fe_3S_4/biochar composites for the efficient degradation of 2,4,6-trichlorophenol: Synergistic effect and mechanism, *J. Environ. Chem. Eng.*, 2020, **10**, 107085.

13 J. Dong, S. Ji, Y. Zhang, M. Ji, B. Wang, Y. Li, Z. Chen, J. Xia and H. Li, Construction of Z-Scheme MnO_2/BiOBr Heterojunction for Photocatalytic Ciprofloxacin Removal and CO_2 Reduction, *Acta Phys. -Chim. Sin.*, 2023, 2212011.

14 X. Meng, G. Peng, Y. Yan, X. Wang, J. Zhu, C. Belver, W. Gong and L. Blaney, Analysis of the steady-state concentrations of reactive species and their role in contaminant degradation by the iron-biochar/persulfate advanced oxidation process: Comparison of probe compound and quenching agent methods, *Sep. Purif. Technol.*, 2025, **354**, 128502.

15 S. Yuan, X. Liu, W. Liao, P. Zhang, X. Wang and M. Tong, Mechanisms of electron transfer from structrual Fe(II) in reduced nontronite to oxygen for production of hydroxyl radicals, *Geochim. Cosmochim. Acta*, 2018, **223**, 422–436.

16 N. Zheng, X. He, R. Hu, R. Wang, Q. Zhou, Y. Lian and Z. Hu, In-situ production of singlet oxygen by dioxygen activation on iron phosphide for advanced oxidation processes, *App. Catal. B*, 2020, **307**, 121157.

17 M. Tan, X. Zheng, W. Yu, B. Chen and C. Chu, Facet-Dependent Productions of Reactive Oxygen Species from Pyrite Oxidation, *Environ. Sci. Technol.*, 2024, **58**, 432–439.

18 K. Li, S. Ma, C. Zou, J. Latif, Y. Jiang, Z. Ni, S. Shen, J. Feng and H. Jia, Unrecognized Role of Organic Acid in Natural Attenuation of Pollutants by Mackinawite (FeS): The Significance of Carbon-Center Free Radicals, *Environ. Sci. Technol.*, 2023, **57**, 20871-20880.

19 Z. Ai, Z. Gao, L. Zhang, W. He and J. J. Yin, Core-Shell Structure Dependent Reactivity of Fe@Fe_2O_3 Nanowires on Aerobic Degradation of 4-Chlorophenol, *Environ. Sci. Technol.*, 2013, **47**, 5344–5352.

20 H. T. Pham, M. Kitsuneduka, J. Hara, K. Suto and C. Inoue, Trichloroethylene Transformation by Natural Mineral Pyrite: The Deciding Role of Oxygen, *Environ. Sci. Technol.*, 2008, **42**, 7470–7475.

21 L. Zhu, H. Wang, J. Sun, L. Lu and S. Li, Sulfur Vacancies in Pyrite Trigger the Path to Nonradical Singlet Oxygen and Spontaneous Sulfamethoxazole Degradation: Unveiling the Hidden Potential in Sediments, *Environ. Sci. Technol.*, 2024, **58**, 6753–6762.

22 J. Xu, X. Tan, W. Ding, A. A. Keller and Y. Huang, External oxidant-free remediation of antibiotics: Activation of oxygen molecules to generate hydroxyl radicals using Co-Fe_3S_4 nanoflowers, *Chem. Eng. J.*, 2023, **463**, 142465.

23 C. Wang, W. Li, Z. Zhang, D. Lei, G. Che, C. Gou, J. Zhang and Z. Hao, A novel iron sulfide phase with remarkable hydroxyl radical generation capability for contaminants degradation, *Water Res.*, 2024, **251**, 121166.